

Luminescent Properties of Rare Earth Ions in One-Dimensional Oxide Nanowires

Hongwei Song,* Lixin Yu, LinMei Yang, and Shaozhe Lu

Key Laboratory of Excited State Physics, Changchun Institute of Optics, Fine Mechanics and Physics,
Chinese Academy of Sciences, 16 Eastern South-Lake Road, Changchun 130033, P. R. China

Rare-earth doped one-dimensional oxide nanowires including LaPO_4 , La_2O_3 , and Gd_2O_3 were synthesized by the hydrothermal method. Their luminescent properties including local environments, electronic transitions, energy transfer, and frequency up-conversion luminescence processes were systematically studied. In $\text{LaPO}_4:\text{Eu}$ and $\text{La}_2\text{O}_3:\text{Eu}$ nanowires, different symmetry sites of Eu^{3+} ions were identified, which obviously differed from those of the corresponding micrometer-sized particles. This was attributed to crystal field degeneration in the fringe along the length axis. In $\text{LaPO}_4:\text{Eu}$ nanowires, the electronic transition rate of $^5\text{D}_1-\sum_J^7\text{F}_J$ increased ~ 2 times over that of the zero-dimensional nanoparticles and micrometer-sized particles, which was related to the variation of dipole field induced by shape anisotropy. Considering the nonradiative relaxations, meanwhile, the luminescent quantum efficiency for $^5\text{D}_1-\sum_J^7\text{F}_J$ transitions of Eu^{3+} in nanowires increased 100% over that in nanoparticles and 20% over that in micrometer particles. In $\text{Gd}_2\text{O}_3:\text{Eu}^{3+}$, $\text{LaPO}_4:\text{Ce}^{3+}$, and $\text{LaPO}_4:\text{Tb}^{3+}$ nanowires and micrometer-sized particles, the electronic transition rate of rare earths had only a little variation. In $\text{LaPO}_4:\text{Ce}^{3+}/\text{Tb}^{3+}$ nanowires, the energy transfer rate of $\text{Ce}^{3+} \rightarrow \text{Tb}^{3+}$ decreased 3 times compared to that in micrometer rods. Despite this, the brightness for the $^5\text{D}_4-^7\text{F}_5$ green emissions of Tb^{3+} increased several times due to decreased energy transfer from the excited states higher than $^5\text{D}_4$ to some defect levels. In $\text{Gd}_2\text{O}_3:\text{Er}^{3+}/\text{Yb}^{3+}$ nanocrystals, as the shape varied from nanopapers to nanowires, the relative intensity of up-conversion luminescence of $^2\text{H}_{11/2}/^4\text{S}_{3/2}-^4\text{I}_{15/2}$ and $^4\text{F}_{9/2}-^4\text{I}_{15/2}$ to the infrared down-conversion luminescence of $^4\text{I}_{13/2}-^4\text{I}_{15/2}$ increased remarkably, indicating efficient up-conversion luminescence. Our present results indicate that rare-earth-doped oxide nanowires is a type of new and efficient phosphors.

Keywords: One-Dimensional Nanocrystals, Rare Earths, Electronic Transition, Energy Transfer.

1. INTRODUCTION

It is well-known that the reduction of particle size of crystalline systems results in important modification of their properties, which are different from those of the bulk because of the following special electronic properties: (1) the increase of surface to volume ratio and (2) quantum confinement effect.^{1,2} In 1994, Bhargava et al. reported that the radiative transition rate of Mn^{2+} ions in ZnS nanocrystals (NC) increased 5 orders in comparison with the corresponding micrometer-sized polycrystalline powders, the so-called bulk materials.³ Ever though this result was strongly criticized later, studies on nanosized luminescent semiconductors attracted great interests. Rare earth

(RE) compounds were extensively applied to lighting, field emission displays (FED), cathode ray tubes (CRT), and plasma display panels (PDP), thus the corresponding nanosized materials also attracted much attention.^{4,5} It is expected that the nanosized phosphors can improve not only the luminescent quantum efficiency (QE) but also the resolution of display.

In the earlier years, most of the research on this topic mainly focused on the luminescent properties of zero-dimensional nanoparticles (NP) and some development was achieved. For example, different methods were used to prepare nanosized phosphors, such as solid-state reactions, sol-gel techniques, hydrolysis, laser-heated evaporation, combustion synthesis, etc.⁶⁻⁸ Some special luminescent properties for nanosized phosphors were recognized. Meltzer et al. studied the electron-phonon interaction in

* Author to whom correspondence should be addressed.

Eu_2O_3 NC by spectral hole burning and determined a relationship of T^α ($3 < \alpha < 4$) between homogeneous line width and temperature.^{9,10} They also observed that the radiative lifetime of Eu^{3+} in NCs depended on the refractive index of the surrounding media.¹¹ Tissue et al. reported that the site symmetry of RE in NCs varied with particle size, which was also observed by the other authors later.^{12,13} Wei et al. observed that in the $\text{YBO}_3:\text{Eu}$ NC, the color purity for the red emissions was greatly improved because the intensity ratio of $^5\text{D}_0\text{--}^7\text{F}_2$ to $^5\text{D}_0\text{--}^7\text{F}_1$ was modified.¹⁴ Several papers reported that in NCs, the fluorescent quenching concentration was improved over that in the polycrystals.^{15–17} In addition, the frequency up-conversion luminescence (UCL) in NCs was also studied.^{18–20} Previously, we systematically studied the luminescent properties of zero-dimensional (0D) cubic $\text{Y}_2\text{O}_3:\text{Eu}$ NPs. We reported the dependence of ultraviolet light-induced spectral change on particle size, irradiation wavelength, and intensity and observed the increased electronic transition rate of $^5\text{D}_0\text{--}\Sigma^7\text{F}_J$, $^5\text{D}_1\text{--}\Sigma^7\text{F}_J$ with the decreasing particle size.^{21–25} It should be pointed out that in nanosized RE doped oxide compounds, the expected size confinement effect was seldom observed. And more, the unexpected surface effect generally leads to increased nonradiative relaxation and decreased luminescent QE.

Recently, one-dimensional (1D) devices such as nanowires (NW) and nanotubes received extensive attention in both fundamental and applied studies.^{26–28} They can not only play a crucial role in important future optoelectronic devices,^{27,29} data storage,³⁰ and biochemical and chemical sensors³¹ but also can be used to enrich our understanding of basic quantum mechanics.³² 1D RE compounds also attract considerable attention. For example, the preparation and luminescent properties for some 1D devices such as $\text{LaPO}_4:\text{RE}$ (RE = Eu^{3+} , Tb^{3+}) NW³³ and $\text{Y}_2\text{O}_3:\text{RE}$ nanotubes^{34,35} were reported. This stimulated our great interest in answering the following questions: Is there any special luminescent property for 1D devices? Could the photoluminescent properties for 1D NWs be improved over those of 0D NPs as well as micrometer-sized materials? Very recently, we observed that in $\text{LaPO}_4:\text{Eu}^{3+}$ NWs, the radiative transition rate and the luminescent QE increased compared to those of 0D NP as well as micrometer-sized particles (MP) and micrometer rods (MR).^{36,37} In this paper, we studied systemically the luminescent properties of $\text{LaPO}_4:\text{RE}$ (RE = Tb^{3+} , Ce^{3+} , Eu^{3+}), $\text{La}_2\text{O}_3:\text{Eu}^{3+}$, and $\text{Gd}_2\text{O}_3:\text{Er}^{3+}/\text{Yb}^{3+}$ NWs, including their crystal field and local environment, electronic transitions, energy transfer (ET), UCL, etc.

2. EXPERIMENTAL DETAILS

2.1. Sample Preparation

The $\text{LaPO}_4:\text{RE}$ (RE = Eu^{3+} , Ce^{3+} , Tb^{3+}) NPs and NWs were both prepared by the wet chemical synthesis technique, which was first reported by H. Messamy et al.³³

In the synthesis, appropriate amounts of La_2O_3 and Eu_2O_3 (1:0.05 mole ratio) were dissolved into concentrated HNO_3 solution and distilled water was added. Then $(\text{NH}_4)_2\text{HPO}_4$ solution (0.18 M) was added into the solution. The pH value of the mixed solution was adjusted to 12–13 (for NP) or 1–2 (for NW). After it was well-stirred, the colloid solution was poured into Teflon-lined autoclaves and heated subsequently at 120 °C for 3 h. The obtained suspension was centrifuged and supernatant was discarded. The resultant precipitation was washed with distilled water and dried at 50 °C. $\text{LaPO}_4:\text{RE}$ MP and MR were prepared by the same method at 150 °C. The practical concentration of Eu^{3+} ions in matrix, as obtained by the plasma spectra method, was found to be 4.15% NP, 4.32% NW, 4.36% MP, and 4.41% MR (in mol %).

In the preparation of 1D $\text{La}_2\text{O}_3/\text{Gd}_2\text{O}_3:\text{RE}$ (RE = Eu^{3+} , Er^{3+} , Yb^{3+}), appropriate amounts of high-purity $\text{La}_2\text{O}_3/\text{Gd}_2\text{O}_3$ and RE_2O_3 were dissolved into concentrated HNO_3 according to the molar ratio. Then appropriate volume of dilute NaOH solution was added to the nitrate solution to obtain $\text{La}(\text{OH})_3$. Diluted NaOH solution (1 M) was used to adjust the pH value in the range of 7–13 for $\text{La}(\text{OH})_3$. After it was well-stirred, the milky colloid solution was obtained and poured into several closed Teflon-lined autoclaves. The $\text{La}(\text{OH})_3/\text{Gd}(\text{OH})_3$ colloidal solution was heated at 120 and 150 °C for 24 h. The obtained suspension was centrifuged at 2770g for 15 min and the supernatant including by-products was discarded. The white precipitation obtained was washed and dried at 50 °C under vacuum. The dried $\text{La}(\text{OH})_3/\text{Gd}(\text{OH})_3$ powders were calcined at 500 °C for 2 h, then $\text{La}_2\text{O}_3/\text{Gd}_2\text{O}_3$ powders were obtained.

2.2. Measurements

Crystal structure, morphology, and size were obtained by X-ray diffraction (XRD) using a Cu target radiation resource (Cu $K\alpha = 1.54078 \text{ \AA}$), transmission electron micrograph (TEM), and scanning electron micrograph (SEM) utilizing a JEM-2010 electron microscope. Fluorescence and excitation spectra were recorded on a Hitachi F-4500 spectrophotometer equipped with a 150-W Xe arc lamp at room temperature, and for comparison of different samples, the emission spectra were measured at a fixed bandpass of 0.2 nm with the same instrument parameters (2.5 nm for excitation split, 2.5 nm for emission split, and 700 V for PMT voltage). In the measurements of fluorescent dynamics and high-resolution spectra of $\text{Eu}^{3+}/\text{Tb}^{3+}$ at low temperatures, the samples were put into a liquid helium cycling system, where the temperature varied from 10 to 300 K. A 266/355-nm light generated from the fourth-harmonic-generator/third-harmonic-generator pumped by the pulsed Nd:YAG laser (line width, 1.0 cm^{-1} ; pulse duration, 10 ns; repetition frequency, 10 Hz) was used as excitation source. The spectra were recorded by a Spex-1403 spectrometer, a photomultiplier,

and a boxcar integrator and processed by a computer. The fluorescence dynamics of Ce^{3+} was measured with a FL920 single-photon spectrometer using a nanosecond flash lamp (pulse width, 1 ns; repetition rate, 40 kHz) as excitation source. In the measurements of up-conversion luminescence, a 980-nm diode laser was used as excitation source. A TR550 grating spectrometer (produced by JY Co., France) was used for detection (200–1700 nm).

3. RESULTS AND DISCUSSION

3.1. Crystal Structure and Morphology

Figure 1 shows TEM and SEM images of $\text{LaPO}_4:\text{Eu}$ powders prepared under different conditions. As can be seen, the morphology of the particles is strikingly different for the two preparation methods: colloids prepared under strongly alkaline comprise particles, while the preparation in acidic solution yields wires. The sizes of the particles prepared at 120 and 150 °C were ~ 20 nm and 2–3 μm , respectively. The length and width of the NW both increased with elevated synthesis temperature (120–150 °C), and the width increased much faster than the length, leading to a decrease in the ratio of length to width. The high-resolution TEM image showed that the inside

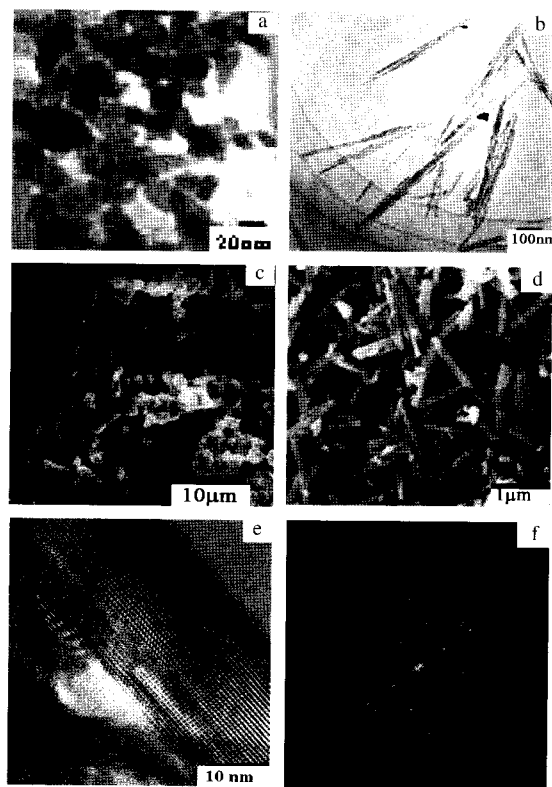


Fig. 1. TEM and SEM images of $\text{LaPO}_4:\text{Eu}$ powders prepared under different conditions. (a) NP:PH = 13, $T = 120$ °C; (b) NW:PH = 1, $T = 120$ °C; (c) MP:PH = 3, $T = 150$ °C; (d) MR:PH = 1, $T = 150$ °C; (e) high-resolution image of (b); (f) electron diffraction patterns of (b).

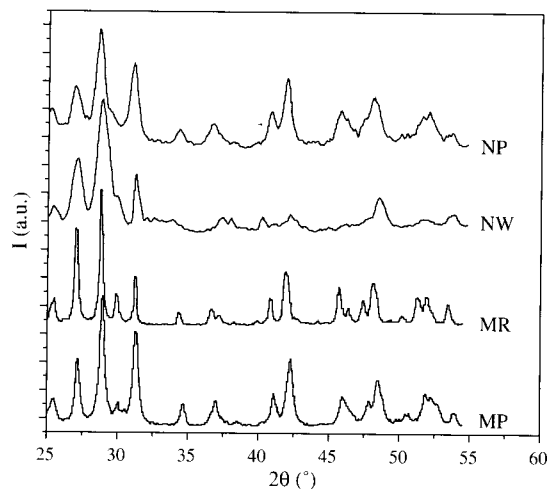


Fig. 2. XRD patterns of $\text{LaPO}_4:\text{Eu}$ powders prepared under different conditions, corresponding to images (a)–(d) in Figure 1.

of the NW was well-crystallized, while the fringe along the length axis degenerated. Electron diffraction pattern showed that the NW was a single crystal. Figure 2 shows the XRD patterns of different $\text{LaPO}_4:\text{Eu}$ powders. Like the LaPO_4 polycrystals prepared with the solid-state reaction, the crystal structures of the samples are all of monoclinic monazite type.^{38,39} In NPs and NWs, the width of the XRD patterns became broader. In NPs and MPs, the relative intensity of XRD patterns had little variation. However, in NWs the relative intensity of the XRD peaks between 40° and 55° became weaker. This was due to the improved shape anisotropy.

Figure 3 shows TEM images of $\text{La}_2\text{O}_3:\text{Eu}$ powders prepared at 120 and 150 °C, respectively. It can be seen that the powders prepared at 120 °C yield wires, with width of 10–20 nm and length of 0.5–1.0 μm . The powders prepared at 150 °C comprise short rods, with width of ~ 100 nm and length of 100–500 nm. Figure 4 shows their XRD patterns. According to XRD patterns, the crystal structures of the samples are both hexagonal, which is the same as that in the polycrystalline materials. Electron diffraction patterns and high-resolution images of TEM demonstrate that the $\text{La}_2\text{O}_3:\text{Eu}$ NW is a single crystal.

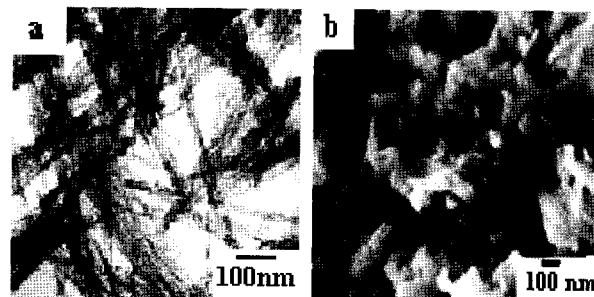


Fig. 3. TEM and SEM images of $\text{La}_2\text{O}_3:\text{Eu}$ (a) NW:PH = 11, $T = 120$ °C; (b) MR:PH = 11, $T = 150$ °C.

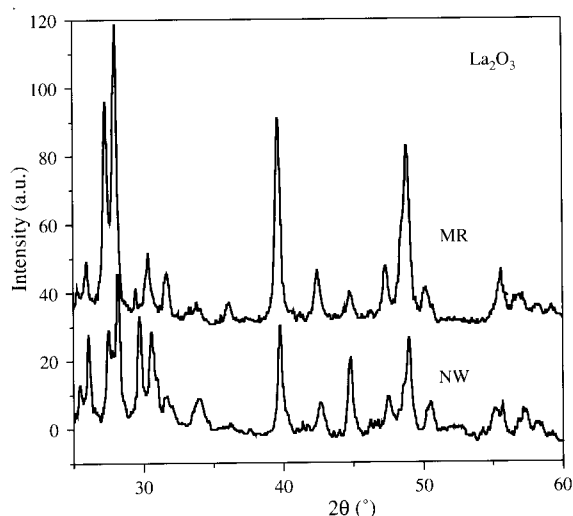


Fig. 4. XRD patterns of $\text{La}_2\text{O}_3:\text{Eu}$ (4%) NW and MR, corresponding to the images (a), (b) in Figure 3.

Figure 5 shows XPD patterns of $\text{Gd}_2\text{O}_3:\text{Eu}$ NC prepared under different conditions. It can be seen that all the samples are in the cubic phase. As the pH value changes, the widths of the XRD peaks have little variation. Estimated from the half-widths of the XRD patterns by the Scherrer's equation, the average crystalline sizes are all ~ 10 – 20 nm. The strength of the XRD patterns in the sample of pH = 13 is higher than that in the other samples, indicating the better crystallinity. Figure 6 shows the TEM images of $\text{Gd}_2\text{O}_3:\text{Eu}$ nanometer powders prepared at different values of pH. As the pH value varied, the morphology of the samples changed significantly. The sample prepared in the solution of pH = 7 yields papers. The sample of pH = 10 mainly contains papers and also a few wires. From (a) and (b) it can be clearly observed that the papers have a depth of ~ 10 – 20 nm and length and width of 50 – 100 nm. The shape of the papers is irregular. The sample of pH = 13 yields wires, with lengths of ~ 1 μm and diameters

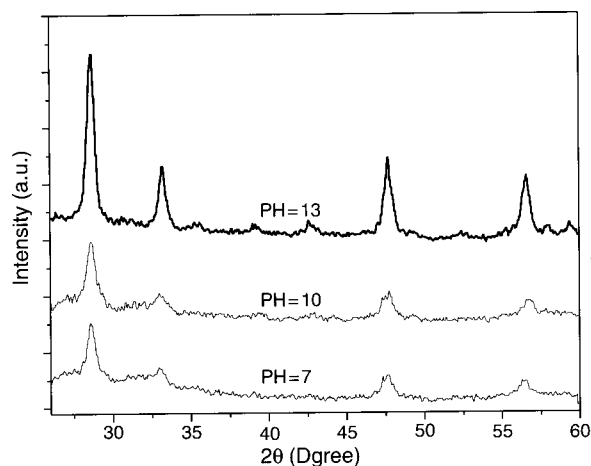


Fig. 5. XRD patterns of $\text{Gd}_2\text{O}_3:2\% \text{Yb}^{3+}, 1\% \text{Er}^{3+}$ (in molar ratio) powders prepared at various pH values.

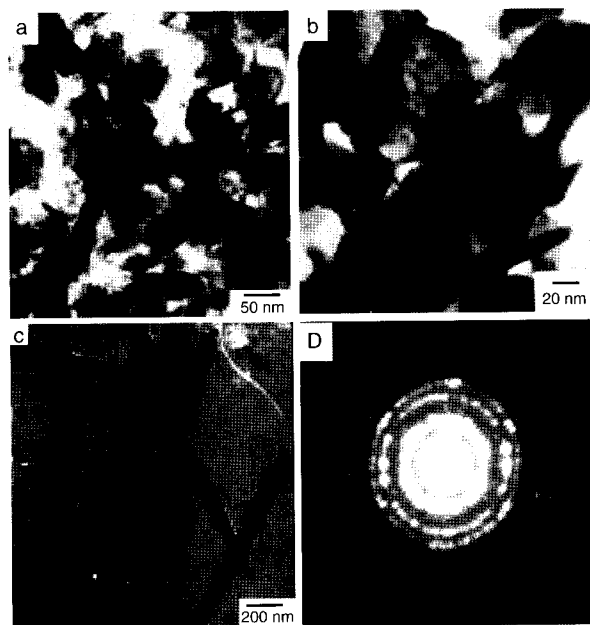


Fig. 6. TEM images of $\text{Gd}_2\text{O}_3:2\% \text{Yb}^{3+}, 1\% \text{Er}^{3+}$ powders (in molar ratio) prepared under various conditions: (a) pH = 7, $T = 130$ $^{\circ}\text{C}$; (b) pH = 10, $T = 130$ $^{\circ}\text{C}$; (c) pH = 13, $T = 130$ $^{\circ}\text{C}$; (d) electron diffraction patterns of (c).

of several tens of nanometers. Note that either the Gd_2O_3 nanosized papers or the nanowires congregated to different contents. The electron diffraction experiments demonstrate that all the samples belong to multicrystals.

3.2. Local Structure Studied by High-Resolution Spectra

3.2.1. Local Structure in $\text{LaPO}_4:\text{Eu}^{3+}$ Nanowires

LaPO_4 belongs to monazite type. In LaPO_4 systems, La^{3+} ions occupy C_1 point group. In Eu^{3+} -doped LaPO_4 , Eu^{3+} ions substitute for some of La^{3+} ions. As known, the $^5\text{D}_0$ – $^7\text{F}_1$ transitions are hypersensitive to the crystal field. $^7\text{F}_1$ in one symmetry site can split into three Stark levels ($2J+1$). On one hand, different symmetry sites results in different groups of emission lines. On the other hand, the variation of local environments surrounding Eu^{3+} in unperfected crystals also results in the shift of Stark lines. Sometimes it is difficult to distinguish the two conditions. Figure 7 shows the high-resolution spectra of different $\text{LaPO}_4:\text{Eu}$ powders at 10 K. In the NP, three $^5\text{D}_0$ – $^7\text{F}_1$ emission lines appeared (L1–L3). In the NW, besides the same lines 1–3, three additional lines 4–6 also appeared. The $^5\text{D}_0$ – $^7\text{F}_1$ lines in the MPs are entirely identical with those of the NPs, indicating that site symmetry in MPs is same as that in NPs. Like NWs, lines 1–6 also appeared in MRs. However, the relative intensity of lines 4–6 in the MRs became weaker in comparison to that in NWs. The results in Figure 7 indicated that in NPs and MPs the $^5\text{D}_0$ – $^7\text{F}_1$ transitions came from one crystalline site, A, while in NWs and MRs the $^5\text{D}_0$ – $^7\text{F}_1$ transitions came from the same site

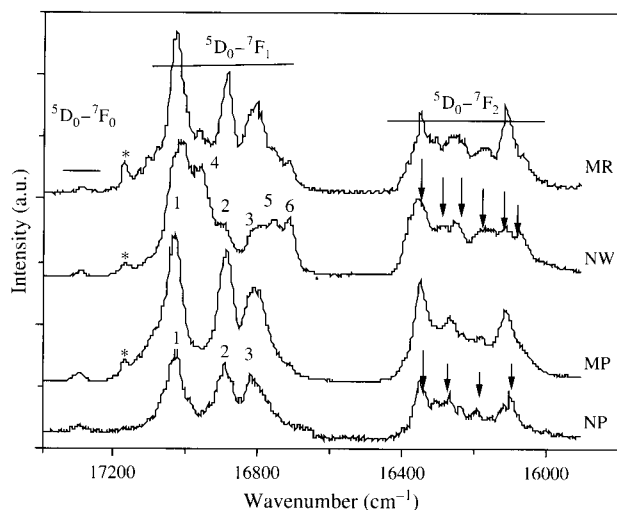


Fig. 7. High-resolution spectra of different $\text{LaPO}_4:\text{Eu}$ powders at 10 K under the 266-nm excitation.

(L1–L3), A, and an additional site (L4–L6), B. The relative number of Eu^{3+} occupying site B decreased as the powders changed from a NW to the a MR. Note that the peaks labeled with a star in Figure 7 were not associated with the $^5\text{D}_0\text{--}^7\text{F}_1$ transitions, but with $^5\text{D}_1\text{--}^7\text{F}_4$ transitions, which was confirmed according to time-resolved emission spectra and the energy levels of $\text{LaPO}_4:\text{Eu}^{3+}$.

The $^5\text{D}_0\text{--}^7\text{F}_2$ emissions in one symmetry site can split into at most five lines in the crystal field. In Figure 7, the Stark lines of the $^5\text{D}_0\text{--}^7\text{F}_2$ emissions were not completely identified because they overlapped each other to some extent. The site-selective excitation experiments were further performed. Parts a and b of Figure 8 show respectively the $^7\text{F}_0\text{--}^5\text{D}_0$ excitation spectra monitoring different $^5\text{D}_0\text{--}^7\text{F}_2$ sites and the $^5\text{D}_0\text{--}^7\text{F}_2$ emission spectra selectively exciting

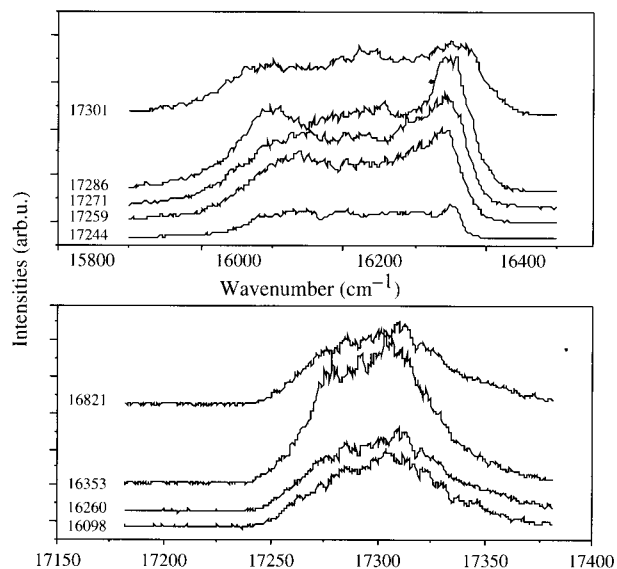


Fig. 8. (a) $^7\text{F}_0\text{--}^5\text{D}_0$ excitation spectra monitoring different $^5\text{D}_0\text{--}^7\text{F}_2$ sites and (b) the $^5\text{D}_0\text{--}^7\text{F}_2$ emission spectra selective exciting $^7\text{F}_0\text{--}^5\text{D}_0$ transitions in $\text{LaPO}_4:\text{Eu}$ NP.

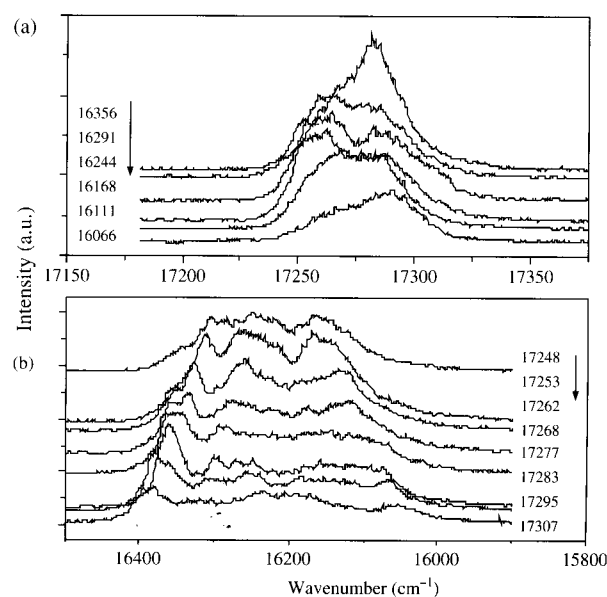


Fig. 9. (a) The $^7\text{F}_0\text{--}^5\text{D}_0$ excitation spectra monitoring different $^5\text{D}_0\text{--}^7\text{F}_2$ sites and (b) the $^5\text{D}_0\text{--}^7\text{F}_2$ emission spectra selective exciting $^7\text{F}_0\text{--}^5\text{D}_0$ transitions in $\text{LaPO}_4:\text{Eu}$ NW.

$^7\text{F}_0\text{--}^5\text{D}_0$ transitions in NPs. As seen, no matter which location was monitored, only one excitation peak appeared. Corresponding to different excitation energies, the emission peaks were nearly same. This indicated that the $^5\text{D}_0\text{--}^7\text{F}_2$ emissions in NP originated from one symmetry site. Parts a and b of Figure 9 show respectively the $^7\text{F}_0\text{--}^5\text{D}_0$ excitation spectra monitoring different $^5\text{D}_0\text{--}^7\text{F}_2$ sites and the $^5\text{D}_0\text{--}^7\text{F}_2$ emission spectra selective exciting $^7\text{F}_0\text{--}^5\text{D}_0$ transitions. In Figure 9a, two different excitation peaks were observed, at $\sim 17\,281$ and $\sim 17\,258\text{ cm}^{-1}$, respectively. They had a little shift with monitoring location. Corresponding to site selective excitation, two groups of emission peaks of $^5\text{D}_0\text{--}^7\text{F}_2$ appeared, indicating that the $^5\text{D}_0\text{--}^7\text{F}_2$ transitions in NW originated from two different sites.

From MPs to NPs (20 nm) the ratio of surface to volume varied greatly, but the site symmetry was the same. In NWs, even though the ratio of surface to volume did not decrease compared to that of the NP, Eu^{3+} occupied the additional site B. Apparently, the appearance of an additional site B is not due to the surface effect but is due to the shape anisotropy. According to the high-resolution TEM images of $\text{LaPO}_4:\text{Eu}$ NWs, the internal atoms arrange trimly, and the arrangement of the atoms in the fringe along the length direction degenerated. This will lead the crystal field surrounding Eu^{3+} in the fringe to be different from that in the interior, causing to the appearance of the new site B. The crystal degeneration in the fringe of the NW is probably related to the sample preparation conditions.

3.2.2. Symmetry Site in the $\text{La}_2\text{O}_3:\text{Eu}^{3+}$ NW

La_2O_3 is hexangular. In Eu^{3+} -doped La_2O_3 , Eu^{3+} ions substitute for some of La^{3+} ions and locate at a C_3 symmetry site.⁴⁰ Parts a and b of Figure 10 show respectively

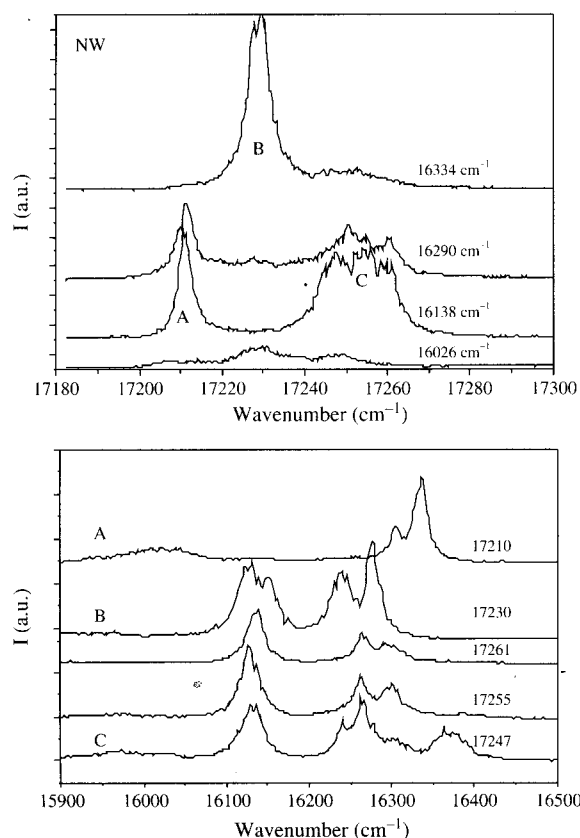


Fig. 10. (a) 7F_0 - 5D_0 excitation spectra monitoring different 5D_0 - 7F_2 sites and (b) the 5D_0 - 7F_2 emission spectra selective exciting 7F_0 - 5D_0 transitions in La_2O_3 :Eu NW.

the 7F_0 - 5D_0 excitation spectra monitoring different 5D_0 - 7F_2 sites and the 5D_0 - 7F_2 emission spectra selective exciting 7F_0 - 5D_0 transitions in NWs. In Figure 10a, as monitoring 16 190 or 16 238 cm^{-1} , two intense excitation peaks appeared, located at 17 210 cm^{-1} (called A) and 17 255 cm^{-1} (called C), respectively. As monitored at 16 334 cm^{-1} , an intense excitation peak located at 17 230 cm^{-1} (called B) and a weak peak around $\sim 17 255 \text{ cm}^{-1}$ (C) were observed. As monitored at 16 026 cm^{-1} , the three peaks, A, B, and C all appeared; however, their intensities were quite weak. Peaks A and B were relatively sharp, while peak C was relatively wide. The above excitation spectra indicate that in the NWs at least three symmetry sites appeared. We suggest that site C probably originates from Eu^{3+} ions in the fringe edge, while sites A and B are from the interior. In the fringe edge, the local environments surrounding Eu^{3+} became disordered in comparison to the interior, thus the emission lines were broadened inhomogeneously. In Figure 10b, on exciting A, B, and C, different groups of emission lines were discerned. Especially, on exciting different locations of C, 17 261, 17 255, and 17 247 cm^{-1} , the emission spectra are different, indicating that C consists of different spectral components.

Parts a and b of Figure 11 show respectively the 7F_0 - 5D_0 excitation spectra monitoring different 5D_0 - 7F_2 sites

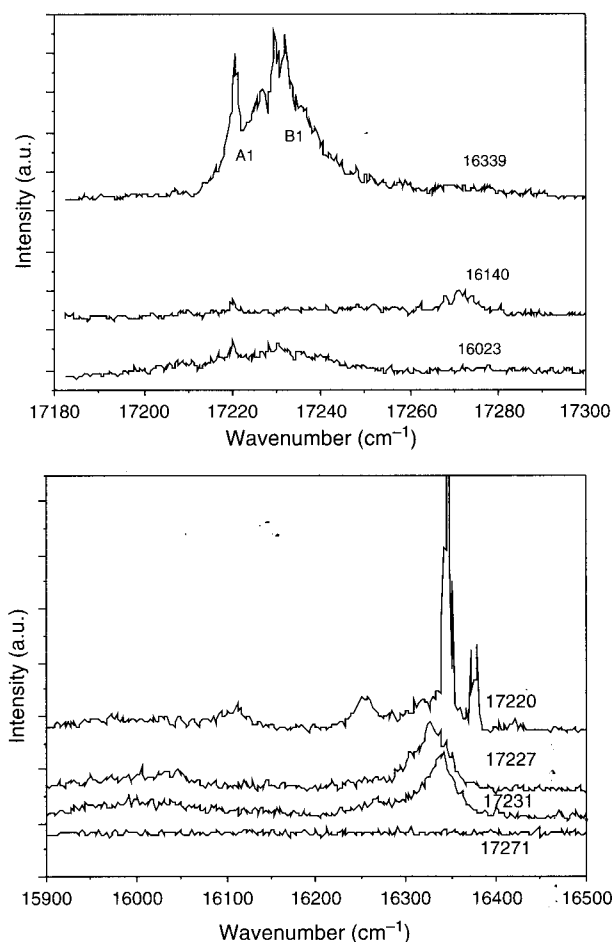


Fig. 11. (a) The 7F_0 - 5D_0 excitation spectra monitoring different 5D_0 - 7F_2 sites and (b) the 5D_0 - 7F_2 emission spectra selective exciting 7F_0 - 5D_0 transitions in La_2O_3 :Eu MR.

and the 5D_0 - 7F_2 emission spectra selective exciting 7F_0 - 5D_0 transitions in MRs. In Figure 11a, on monitoring 16 339 cm^{-1} , two intense excitation peaks located at 17 220 cm^{-1} (A1) and 17 235 cm^{-1} (A2) were observed. A1 is fairly sharp and B1 is quite wide. They overlapped to some extent. On monitoring 16 140 cm^{-1} , a weak peak located at 17 271 cm^{-1} was observed. However, no emission line was observed corresponding to excitation at 17 271 cm^{-1} , indicating that the line probably come from noise. In Figure 11b, as exciting A and B locations, two groups of emission lines were discerned. In comparison to the excitation and emission spectra in Figure 10, it is obvious that the site A1 or B1 in MRs differs from site A, B, or C in NWs. Therefore, we can conclude that the site symmetry in La_2O_3 NW varied greatly from that in La_2O_3 MR.

3.3. Electronic Transition Rates

3.3.1. Electronic Transition Rates in LaPO_4 :Eu

It is significant to study the radiative and nonradiative transition processes of RE ions, which yield the luminescent QE. Here we try to compare the radiative and nonradiative

transition processes of Eu^{3+} in different powders. For Eu^{3+} ions, $^5\text{D}_1$ is an intermediate excited state among $^5\text{D}_J$ and thus is suitable to analyze the transition processes. The lifetime of $^5\text{D}_1$ can be expressed as³⁶

$$\tau(T) = \frac{1}{W_1 + W_{10}(T)} \quad (1)$$

where W_1 is the radiative transition rate of $^5\text{D}_1 \rightarrow \sum_J ^7\text{F}_J$, $W_{10}(T)$ is the nonradiative transition rate of $^5\text{D}_1 \rightarrow ^5\text{D}_0$ at a certain temperature, T . Here, the cross-relaxation processes and the charge-transfer processes of $^5\text{D}_1$ -CTS (charge-transfer state) have been neglected. In our experiments, the lifetimes of $^5\text{D}_1$ hardly changed for different concentrations of Eu^{3+} , indicating the absence of cross-relaxation. According to the theory of multiphonon relaxation, the lifetime of $^5\text{D}_1$ can be expressed as

$$\tau = \frac{1}{W_1 + W_{10}(0)[1 - \exp(-\hbar\omega/kT)]^{-\Delta E_{10}/\hbar\omega}} \quad (2)$$

where $W_{10}(0)$ is nonradiative transition rate at 0 K, ΔE_{10} is the energy separation between $^5\text{D}_1$ and $^5\text{D}_0$, $\hbar\omega$ is the phonon energy, and k is Boltzmann's constant. According to Eq. 2, if the fluorescence lifetime as a function of temperature is experimentally determined, then the radiative and nonradiative transition rate can be obtained by fitting.

The fluorescence decay curves of $^5\text{D}_1 \rightarrow ^7\text{F}_1$ in different $\text{LaPO}_4:\text{Eu}$ powders were measured at different temperatures. Figure 12 shows the dependence of $^5\text{D}_1 \rightarrow ^7\text{F}_1$ exponential lifetimes on temperature. It can be seen that the fluorescence lifetime reserved as a constant below a certain temperature and then became shorter as the temperature was elevated continuously. The experimental data were well fitted by Eq. 2. In the fitting, we choose $\Delta E_{10} = 1758 \text{ cm}^{-1}$, $\hbar\omega = 390 \text{ cm}^{-1}$ for all the samples. In different powders, the locations of the energy levels of Eu^{3+} have

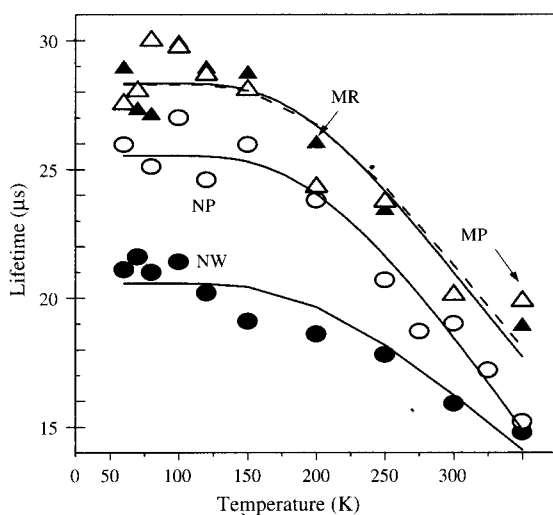


Fig. 12. Dependence of $^5\text{D}_1 \rightarrow ^7\text{F}_1$ fluorescence lifetime at $18\,070 \text{ cm}^{-1}$ on temperature in various $\text{LaPO}_4:\text{Eu}$ powders. Scattered dots are experimental data and solid lines are fitting functions.

only a little variation, which hardly influences the calculation results. According to Raman spectra, the vibration mode at 390 cm^{-1} is the strongest one in different LaPO_4 powders. By fitting, W_1 and $W_{10}(0)$ at different powders were found to be 14.9 and 24.1 ms^{-1} in the NP, 28.9 and 19.7 ms^{-1} in the NW, 17.6 and 17.8 ms^{-1} in the MP, and 16.5 and 18.5 ms^{-1} in the MR. It is apparent that the radiative transition rate $^5\text{D}_1 \rightarrow \sum_J ^7\text{F}_J$ in the MP and the MR is nearly same. The radiative transition rate in the NPs had only a little variation in comparison to the MP and MR, while that in the NW increased 63%. In comparison to the MP and MR, the nonradiative transition rate of $^5\text{D}_1 \rightarrow ^5\text{D}_0$ in the NP increased $\sim 25\%$ and in the NW had only a little increase. The luminescent QE for the $^5\text{D}_1$ level at 0 K, dominated by $\text{QE} = W_1/[W_1 + W_{10}(0)]$, was thus determined to be 59, 30, 49, 47%, respectively, in the NW, NP, MP, and MR. It is obvious that the QE of Eu^{3+} in the NW increased compared to that in the NP, MP, and MR. Assuming that the luminescent QE of $^5\text{D}_0$ is close to 1 for all the samples and the electronic populations fed from CTS to $^5\text{D}_0$ and $^5\text{D}_1$ hardly change in different samples, then the intensity ratio of $^5\text{D}_1 \rightarrow \sum_J ^7\text{F}_J / ^5\text{D}_0 \rightarrow \sum_J ^7\text{F}_J$ can be used to compare the QE of $^5\text{D}_1$ in different samples roughly. We measured the emission spectra and compared the intensity ratio of $^5\text{D}_1 \rightarrow \sum_J ^7\text{F}_J / ^5\text{D}_0 \rightarrow \sum_J ^7\text{F}_J$ in the NW and NP and observed that the intensity of $^5\text{D}_1 \rightarrow \sum_J ^7\text{F}_J / ^5\text{D}_0 \rightarrow \sum_J ^7\text{F}_J$ in the NW is larger, suggesting that the QE of $^5\text{D}_1$ in the NW is higher. This result is quantitatively in accordance with the calculated QE of $^5\text{D}_1$ through the fluorescence dynamics.

The fluorescence lifetime of the $^5\text{D}_0 \rightarrow ^7\text{F}_2$ transition as a function of temperature (10–300 K) in different samples was also measured. As the temperature varied from 10 to 300 K, the $^5\text{D}_0$ lifetimes in all samples hardly changed. The lifetime of $^5\text{D}_0 \rightarrow ^7\text{F}_2$ at room temperature (at $16\,342 \text{ cm}^{-1}$) was found to be 2.25 ms in the NP, 1.63 ms in the NW, 2.32 ms in the MP, and 2.40 ms in the MR. The $^5\text{D}_0$ is the lowest excited state and the energy separation between $^5\text{D}_0$ and the nearest lower level $^7\text{F}_6$ is as high as $\sim 12\,000 \text{ cm}^{-1}$. In this case, nonradiative relaxation processes hardly happens according to the theory of multiphoton relaxation. Thus we suppose that the radiative transition rate of $^5\text{D}_0 \rightarrow \sum_J ^7\text{F}_J$ equals the inverse of the fluorescence decay time. Then we deduced the radiative transition rate of $^5\text{D}_0 \rightarrow \sum_J ^7\text{F}_J$ to be 0.61 cm^{-1} in the NW, 0.44 cm^{-1} in the NP, 0.43 ms^{-1} in the MP, and 0.42 ms^{-1} in the MR. It is obvious that the radiative transition rate of $^5\text{D}_0 \rightarrow \sum_J ^7\text{F}_J$ in the NW also increased compared to that in the other samples.

For RE ions, the diameter of the electronic wavefunction of f -electron is on the order of 10^{-1} nm , which is much smaller than the particle diameter, indicating the absence of confinement effects.²³ The improved transition rate in NW can be discussed by the following formula,¹¹

$$\tau_R = \frac{1}{f(ED)} \frac{\lambda_0^2}{[1/3(n^2 + 2)]^2 n} \quad (3)$$

where τ_R is the radiative fluorescence lifetime, $f(ED)$ is the oscillator strength of electronic dipole transition, λ_0 is the wavelength in vacuum, and n is the refractive index of the samples. First, the radiative fluorescence lifetime strongly depends on the oscillator strength of the electronic dipole transition, $f(ED)$. $f(ED)$ is strongly dependent on the crystal field and the electronic/magnet dipole field surrounding Eu^{3+} ions. The shape anisotropy will hardly influence the crystal field, but will influence the dipole field caused by the excited ion. The latter is not only influenced by the typical dimensions and dielectric constants of the host particles but also by their shape. We suggest that the shape anisotropy affects the ionic dipole field and therefore the photonic density of states and thus the radiative transition rate. In addition, Meltzer et al. reported that the radiative fluorescence lifetime of $\text{Y}_2\text{O}_3:\text{Eu}$ nanocrystals is dependent on not only the refractive index itself but also the surrounding medium.¹⁷ They defined that, in nanocrystals, n in Eq. 3 should be substituted by the effective refractive index $n_{\text{eff}} = xn + (1-x)n_{\text{med}}$, where x is the “filling factor” showing what fraction of space is occupied by the nanocrystals and n_{med} is refractive index of medium. In our work, the lifetime was obtained under vacuum conditions, thus $n_{\text{med}} = 1$. In light of the definition of x , we assume x is equal to 1 in polycrystalline powders and x is less than 1 in the NPs and NWs. Accordingly, the radiative lifetime in NPs and NWs should both become longer than that of the micrometer powders ($n > 1$). However, the experimental results differ from this point, suggesting that the change of effective index is not the main factor leading the change of radiative transition rate in different samples.

In NPs and NWs the nonradiative transition rate increased compared to that in the micrometer-sized powders with different content. This can be attributed to the surface effect. On the surface, a large number of defects generally exist, which act as the nonradiative transition channels, leading the nonradiative transition rates to increase. The simple calculation demonstrates that the ratio of the surface atoms to the volume atoms is $\sim 1\%$ in MPs and MRs, $\sim 10\%$ in NWs, and $\sim 20\%$ in NPs. Thus the calculation of the nonradiative transition rate is qualitatively in accordance with the geometrical properties.

3.3.2. Electronic Transition Rates in $\text{Gd}_2\text{O}_3:\text{Eu}$

The dependence of the fluorescence lifetime on temperature for the ${}^5\text{D}_1\text{--}{}^7\text{F}_1$ emissions in $\text{Gd}_2\text{O}_3:\text{Eu}$ powders was also measured, as shown in Figure 13. It can be seen that the lifetime for NWs is a little bit longer than that for MRs, indicating that the sum of the radiative and nonradiative transition rates is a little bit smaller. Unlike the LaPO_4 series, the lifetime from 10 to 300 K had only a little variation. Therefore, it is hard to accurately determine W_1 and $W_{10}(0)$. Despite this, we fitted experimental data with Eq. 2. By fitting, W_1 was determined to be $5.4 \pm 1.2 \text{ ms}^{-1}$ in NWs and $4.8 \pm 0.9 \text{ ms}^{-1}$ in MRs. $W_{10}(0)$

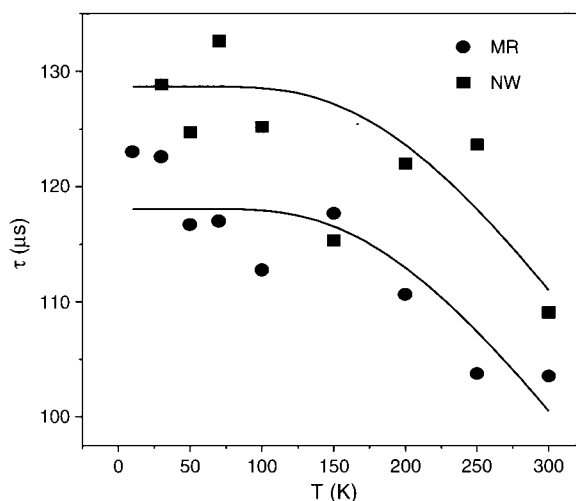


Fig. 13. Dependence of ${}^5\text{D}_1\text{--}{}^7\text{F}_2$ fluorescence lifetime at $18\,070 \text{ cm}^{-1}$ on temperature in various $\text{La}_2\text{O}_3:\text{Eu}$ powders. Scattered dots are experimental data and solid lines are fitting functions.

was determined to be $3.7 \pm 0.9 \text{ ms}^{-1}$ in NWs and $2.6 \pm 1.1 \text{ ms}^{-1}$ in MRs. Considering the experimental errors, the radiative transition rate had hardly change. The nonradiative transition rate might have increased a little. Further work should be performed in a broader temperature range.

The ${}^5\text{D}_0\text{--}{}^7\text{F}_2$ fluorescence lifetimes in La_2O_3 NWs and MRs were also measured. At 10 K, the fluorescence lifetimes in NWs and MR were determined to be 0.82 and 0.73 ms, respectively. Neglecting the nonradiative transition rate, then the radiative transition rate can be obtained to be 1.22 ms^{-1} in NWs and 1.38 ms^{-1} in MRs. Unlike in $\text{LaPO}_4:\text{Eu}$, the radiative transition rate in Gd_2O_3 has only changed a little between NWs and MRs. The following experiments will demonstrate that in $\text{LaPO}_4:\text{Ce}^{3+}$ and $\text{LaPO}_4:\text{Tb}^{3+}$ NWs and BRs the radiative transition rate also has only a little variation. This means that the variation of radiative transition rate in NWs should be dependent on the host materials and the crystal lattice, the RE ions and their site symmetry, etc. The essential for this should be realized further.

3.4. Electronic Transition and ET Processes in $\text{LaPO}_4:\text{Ce}^{3+}/\text{Tb}^{3+}$

In many phosphors, efficient photoluminescence was obtained through ET between donor and acceptor pairs, such as Ce^{3+} and Tb^{3+} , Yb^{3+} , and Er^{3+} , etc., which was widely studied in the polycrystalline materials. In ET systems, as the particle size decreased from micrometer scale to nanometer scale, how does the ET process change? Recently, we experimentally studied the ET processes in $\text{LaPO}_4:\text{Ce}^{3+}$, Tb^{3+} NWs and MRs. Parts a, b, and c of Figure 14 show respectively the excitation and emission spectra in Ce^{3+} - and Tb^{3+} -activated and $\text{Ce}^{3+}/\text{Tb}^{3+}$ coactivated LaPO_4 powders. In Figure 14a, the excitation bands consist of three components with maximums at 241, 258,

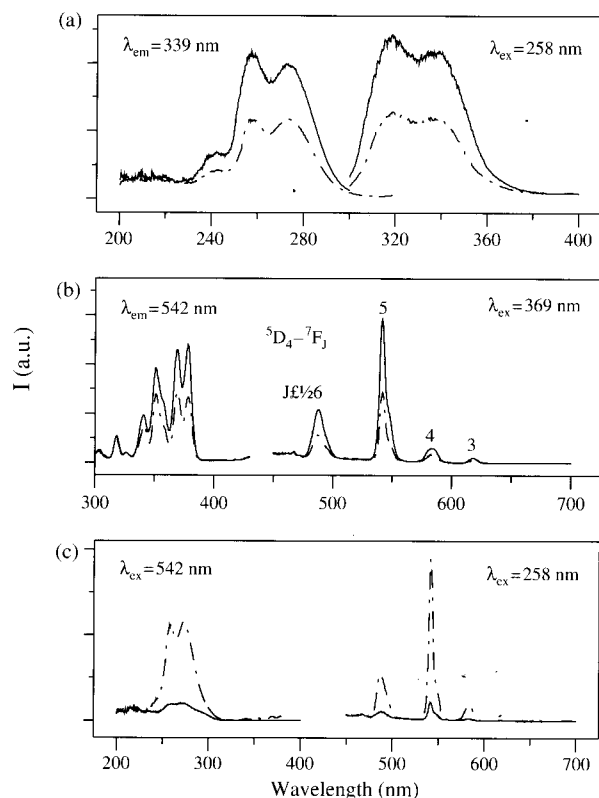


Fig. 14. (a) Excitation spectra ($\lambda_{em} = 339$ nm) and emission spectra ($\lambda_{ex} = 258$ nm) in LaPO₄:Ce (1%). (b) Excitation spectra ($\lambda_{em} = 542$ nm) and emission spectra ($\lambda_{ex} = 369$ nm) in LaPO₄:Tb (2.5%). (c) Excitation spectra ($\lambda_{em} = 542$ nm) of LaPO₄:Ce (1%), Tb (2.5%). Solid lines, MR; dash lines, NW.

and 276 nm, which are associated with allowed f-d transitions from the ground-state $^2F_{5/2}$ to different crystal-field components at the 5d level.⁴ The emission band consists of two peaks with maximums at 318 and 340 nm, corresponding to the transitions from the lowest 5d excited state to the spin-orbit components (2D) of the doublet ground state, $^2F_{5/2}$, $^2F_{7/2}$.²³ In Figure 14b, the excitation lines are associated with $^7F_6-^5D_3$, 5G_J , and 5L_6 of Tb³⁺, while the emission lines from 450 to 650 nm are associated with the $^5D_4-^7F_J$ ($J = 3-6$) transitions. In Figure 14c, when monitoring the emission of Tb³⁺ at 542 nm, stronger allowed f-d transitions of Ce³⁺ and weaker forbidden f-f transitions of Tb³⁺ ions were observed, implying efficient ET from Ce³⁺ to Tb³⁺ ions. The intensity of Tb³⁺ originated from Ce³⁺ \rightarrow Tb³⁺ ET excitation is 2 orders higher than that from the f-f transitions of Tb³⁺.

Parts a and b of Figure 15 show respectively the dependence of the $^5D_4-^7F_5$ emission intensity of Tb³⁺ and the ET efficiency of Ce³⁺ \rightarrow Tb³⁺ on concentration of Tb³⁺ in LaPO₄:Ce³⁺/Tb³⁺ powders. The ET efficiency from a donor (Ce³⁺) to an acceptor (Tb³⁺) was calculated according to the formula $\eta_{ET} = 1 - I_d/I_{d0}$, where I_d and I_{d0} were, respectively, the corresponding luminescence donor intensity in the presence and absence of the acceptor for the same donor concentration. The ET efficiency for both

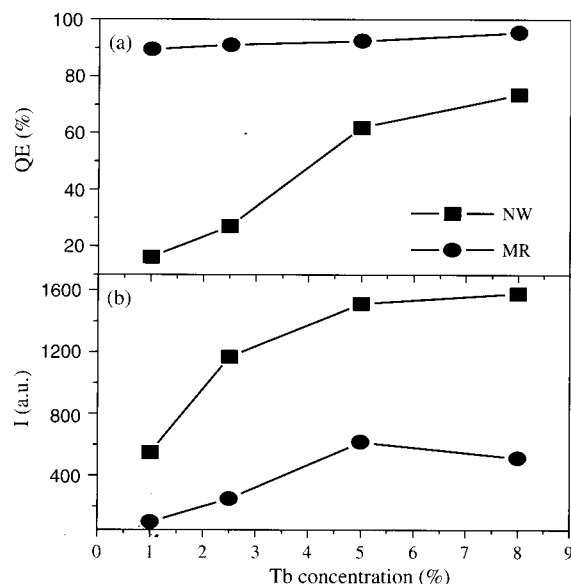


Fig. 15. Dependence of ET efficiency (a) and emission intensity (b) of the $^5D_4-^7F_5$ transitions through ET excitation ($\lambda_{ex} = 258$ nm) of Ce³⁺ \rightarrow Tb³⁺ on Tb³⁺ concentration in LaPO₄:Ce³⁺ (1%)/Tb³⁺.

NWs and MRs increased with Tb³⁺ concentration, and that in the NWs increased more rapidly. The ET efficiency in NWs decreased compared to that in MRs for any Tb³⁺ concentration. Despite the ET efficiency decrease, the brightness of Tb³⁺ in the NWs increased significantly compared to that in MR.

In Ce³⁺/Tb³⁺ coactivated materials, the brightness of Tb³⁺ through ET excitation was dominated by the following factors: (1) the electronic transition rate and the density of Ce³⁺, (2) the ET rate of Ce³⁺, and (3) the electronic transition rate and density of Tb³⁺. To determine the electronic transition and the ET rates, the fluorescent dynamics of Ce³⁺ and Tb³⁺ were investigated. Figure 16 shows the dependence of fluorescent lifetime of Ce³⁺ on Ce³⁺ and Tb³⁺ concentration. In Figure 16a, the lifetime of Ce³⁺ in the NWs hardly changed, as the concentration of Ce³⁺ varied from 1 to 5% in molar ratio, while that in the MRs decreased with increasing Ce³⁺ concentration. This indicated that the fluorescence quenching concentration for NWs was higher than that for MRs. A similar phenomenon was also observed in RE doped NPs. As has been discussed in the literature, the deficiency of traps due to the limited primitive cells per particle, as well as the hindrance of energy transfer of the particle boundary, should be responsible for the increased quenching concentration with decreased particle size.^{16,17} In Figure 16b, the lifetime of Ce³⁺ in NWs and MRs decreased with the concentration of Tb³⁺ and that in NWs decreased more slowly. The reverse of the lifetime of Ce³⁺ is well-fitted with a linear function

$$\tau^{-1} \propto R_C + R_{ET}[\text{Tb}^{3+}] \quad (4)$$

where R_C is the electronic transition rate of Ce³⁺, including the radiative and nonradiative transitions, and R_{ET}

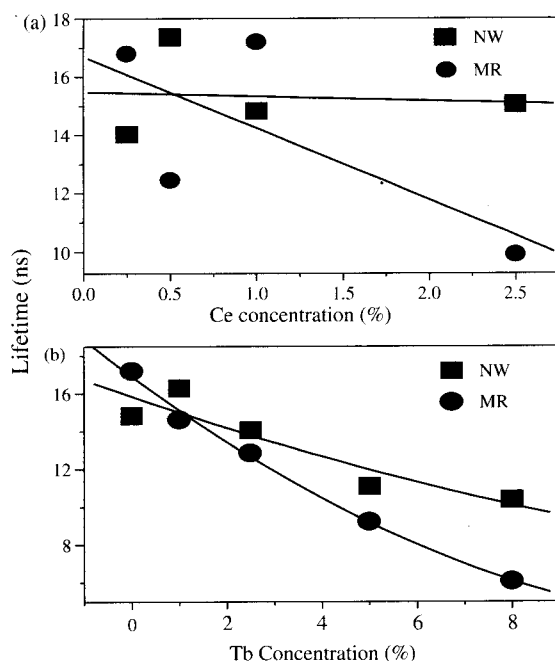


Fig. 16. Dependence of Ce^{3+} lifetime on Ce^{3+} concentration in $\text{LaPO}_4:\text{Ce}^{3+}$ (a) and on Tb^{3+} concentration in $\text{LaPO}_4:\text{Ce}^{3+}$ (1%), Tb^{3+} (b).

is the ET rate. By fitting, R_C was deduced to be $6.3 \times 10^{-2} \text{ ns}^{-1}$ in NWs and $5.2 \times 10^{-2} \text{ ns}^{-1}$ in MRs. R_{ET} was deduced to be $0.44 \text{ ns}^{-1} \text{ mol}^{-1}$ in NWs and $1.30 \text{ ns}^{-1} \text{ mol}^{-1}$ in MRs. The electronic transition rate of Ce^{3+} in NWs increased a little compared to that in MRs, while the ET rate of $\text{Ce}^{3+} \rightarrow \text{Tb}^{3+}$ decreased 3 times.

The $^5\text{D}_4$ - $^7\text{F}_5$ fluorescence decays for Tb^{3+} in $\text{LaPO}_4:\text{Tb}$ NWs and MRs were also compared. The exponential lifetime was determined to be 2.72 ms in NWs and 2.57 ms in MRs. This indicates that the total electronic transition rate of $^5\text{D}_4$ hardly changes in NWs and MRs. In addition, the lifetime of the $^5\text{D}_4$ - $^7\text{F}_5$ lines at different temperatures hardly changes, indicating that the nonradiative relaxation via $^5\text{D}_4$ is negligible, and the reverse of lifetime equals the radiative transition rate of $^5\text{D}_4 \rightarrow \Sigma ^7\text{F}_j$.

The brightness increase for the green emissions in $\text{Ce}^{3+}/\text{Tb}^{3+}$ coactivated NWs was unusual in the case where the electronic transition rate for $\text{Ce}^{3+}/\text{Tb}^{3+}$ had little variation, and the ET rate of $\text{Ce}^{3+} \rightarrow \text{Tb}^{3+}$ in NWs decreased much more than that in MRs. In the $\text{LaPO}_4:\text{Ce}/\text{Tb}$ system, as Ce^{3+} ions were excited, electrons were excited from the ground state $^2\text{F}_{5/2}$ to the $5d$ excited state of Ce^{3+} and feed to some excited states of Tb^{3+} . Then the electrons at higher excited states of Tb^{3+} relax to $^5\text{D}_4$ and generate the $^5\text{D}_4$ - $^7\text{F}_5$ transitions. According to the theory of Foster-Dexter, the energy for $^7\text{F}_6$ - $^3\text{H}_6$ excitation transitions of Tb^{3+} is exactly the same as that for the $5d$ - $^2\text{F}_{5/2}$ emission transitions of Ce^{3+} . The ET between the two donor-acceptor transitions has the largest probability. We guess that after the ET of $\text{Ce}^{3+} \rightarrow \text{Tb}^{3+}$, some energy is lost again at higher levels than $^5\text{D}_4$ through ET from Tb^{3+} to some uncertain defect states near Tb^{3+} . This competitive process

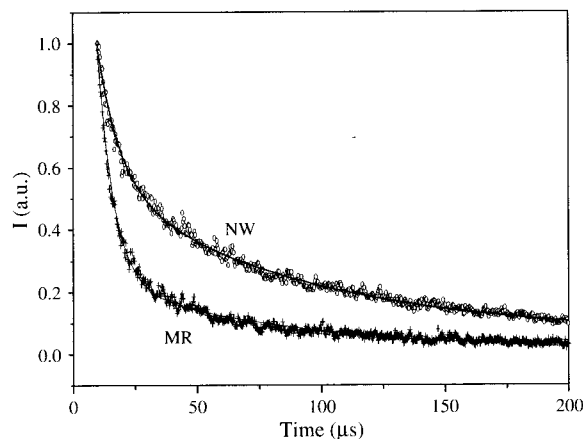


Fig. 17. Fluorescence decay curves of the $^5\text{D}_3$ - $^7\text{F}_5$ transitions in $\text{LaPO}_4:\text{Tb}$ (2.5%) NW and MR.

causes the electron population ultimately arriving in $^5\text{D}_4$ from higher excited states to decrease.

In order to confirm the consideration above, the fluorescence decay processes higher than $^5\text{D}_4$ in NWs and MRs were investigated and compared. Figure 17 shows the decay curves of $^5\text{D}_3$ - $^7\text{F}_5$ in the two powders. As can be seen, the decay curves included two components, a faster and a slower, for both NWs and MRs. They can be well-fitted with a bi-exponential function, $I = I_1 \exp(t/\tau_1) + I_2 \exp(t/\tau_2)$ with $I_1 + I_2 = 1$. The fitting parameters are $I_1 = 0.23$, $\tau_1 = 7.3 \mu\text{s}$, $I_2 = 0.77$, and $\tau_1 = 68 \mu\text{s}$ for NWs and $I_1 = 0.62$, $\tau_1 = 6.8 \mu\text{s}$, $I_2 = 0.77$, and $\tau_1 = 84 \mu\text{s}$. The decay constants of the two components for NWs and MRs did not change much. However, the proportion of the slower component in the NWs became much larger than that in the MRs. We assume that the two components correspond with two processes, the faster to the ET from $^5\text{D}_3$ to the defect states and the slower to the nonradiative relaxation of $^5\text{D}_4$ - $^5\text{D}_3$, because the nonradiative ET rate between a luminescent center of RE and a defect level nearby is much faster than the nonradiative relaxation rate of RE.¹⁵ Therefore, we can claim that the proportion of depopulated electrons in $^5\text{D}_3$ through ET in NWs is much smaller than that in MRs, leading the lower energy loss and the increased brightness of $^5\text{D}_4$ - $^7\text{F}_5$. Here, we did not compare the decay processes in the higher excited states than $^5\text{D}_3$ because the fluorescence was too weak to detect. Now we cannot identify what the defect states near Tb^{3+} are. The formation of defect states may be related to the doping of Ce in the host, because the brightness increase in NWs was only observed in $\text{Ce}^{3+}/\text{Tb}^{3+}$ coactivated LaPO_4 powders and was not observed in Tb^{3+} -doped ones.

The decrease of ET rate for Ce^{3+} to Tb^{3+} and for Tb^{3+} to defect levels essentially should be also attributed to the deficiency of traps due to the limited primitive cells per particle, as well as the hindrance of energy transfer of the particle boundary, as with concentration quenching. The above experiments demonstrate that in NWs as well as the other nanometer materials the ET efficiency decreases

in general. It is not a detrimental thing all the time. The decrease of ET efficiency from the donors to the luminescent acceptors is unexpected. However, the decrease of ET efficiency from the luminescent centers to the defect levels favors photoluminescence. Further work should be performed to compare the ET processes between 1D NWs and 0D NPs both experimentally and theoretically.

3.5. UCL in $\text{Gd}_2\text{O}_3\text{:Yb}^{3+}/\text{Er}^{3+}$ NWs

Since Mastuura et al. reported strong UCL in trivalent RE doped yttria nanocrystals, infrared to visible UCL in nanocrystals has attracted considerable interest due to its potential application in IR detection, molecule recognition, and three-dimensional displays.¹⁸ The UCL in wirelike nanocrystals has not been reported yet, to our knowledge. Figure 18 shows the visible and near-infrared luminescent spectra in $\text{Gd}_2\text{O}_3\text{:Yb}^{3+}/\text{Er}^{3+}$ NWs under 980-nm excitation. In the spectra, green UCL of $^2\text{H}_{11/2}/^4\text{S}_{3/2}-^4\text{I}_{15/2}$, red UCL of $^4\text{F}_{9/2}-^4\text{I}_{15/2}$, and IR emissions of $^4\text{I}_{13/2}-^4\text{I}_{15/2}$ were observed. The IR emissions of $^4\text{I}_{13/2}-^4\text{I}_{15/2}$ gradually decreased with the increase of pH value and the formation of NWs, while the visible UCL of $^2\text{H}_{11/2}/^4\text{S}_{3/2}-^4\text{I}_{15/2}$ and $^4\text{F}_{9/2}-^4\text{I}_{15/2}$ gradually increased. The relative intensity of the green emissions to the red emissions also increased with the increase of pH value. Between the samples prepared at different temperatures, NWs (pH = 13, $T = 130^\circ\text{C}$) and MWs (pH = 13, $T = 170^\circ\text{C}$), the relative intensity of the UCL $^2\text{H}_{11/2}/^4\text{S}_{3/2}-^4\text{I}_{15/2}$ and $^4\text{F}_{9/2}-^4\text{I}_{15/2}$ to IR emissions of $^4\text{I}_{13/2}-^4\text{I}_{15/2}$ had little variation.

Under the 980-nm excitation, ground-state electrons of $^4\text{I}_{15/2}$ were excited into $^4\text{I}_{11/2}$ first via the ground-state absorption or the ET of $\text{Yb}^{3+} \rightarrow \text{Er}^{3+}$. Some electrons in $^4\text{I}_{11/2}$ relaxed to $^4\text{I}_{13/2}$ and the others were excited into $^4\text{F}_{7/2}$ via excited-state absorption or ET and relaxed to

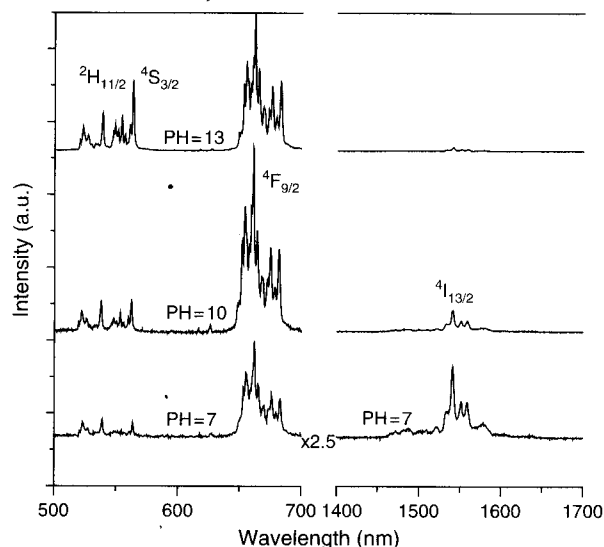


Fig. 18. UCL and near-IR luminescence spectra in $\text{Gd}_2\text{O}_3\text{:2% Yb}^{3+}$, 1% Er^{3+} (molar ratio) NW under 980-nm excitation.

$^2\text{H}_{11/2}/^4\text{S}_{3/2}$, generating the green $^2\text{H}_{11/2}/^4\text{S}_{3/2}-^4\text{I}_{15/2}$ emissions, or relaxed to $^4\text{F}_{9/2}$, generating the red UCL of $^4\text{F}_{9/2}-^4\text{I}_{15/2}$. The electrons in $^4\text{I}_{13/2}$ can transit to $^4\text{I}_{15/2}$, generating the IR emissions of $^4\text{I}_{13/2}-^4\text{I}_{15/2}$, and also can be excited to $^4\text{F}_{9/2}$, generating the red UCL of $^4\text{F}_{9/2}-^4\text{I}_{15/2}$. From the UCL processes we can know that the larger the nonradiative relaxation probability of $^4\text{I}_{11/2}-^4\text{I}_{13/2}$ is, the larger the emission intensity of $^4\text{I}_{13/2}-^4\text{I}_{15/2}$ is, and the smaller the emission intensity of UCL is. Therefore, the intensity ratio of the UCL of $^2\text{H}_{11/2}/^4\text{S}_{3/2}-^4\text{I}_{15/2}$ to IR emissions of $^4\text{I}_{13/2}-^4\text{I}_{15/2}$ is a critical parameter for the QE of UCL. The above experiments demonstrate that as the shape of Gd_2O_3 varied from nanocrystalline papers to NWs, the nonradiative relaxation rate of $^4\text{I}_{11/2}-^4\text{I}_{13/2}$ as well as the other relaxation rate for Er^{3+} became smaller. We consider that as the nanocrystals varied from nanosized papers to NWs, the ratio of volume-to surface become smaller gradually, leading to the decrease of the surface defects, which may act as the nonradiative relaxation channels. In Y_2O_3 nanocrystals, the groups with high-frequency vibrational modes like CO_3^{2-} and OH^- are involved due to surface contamination and they increase with decreasing particle size.^{19,20} The increase of the groups with very high vibration energies

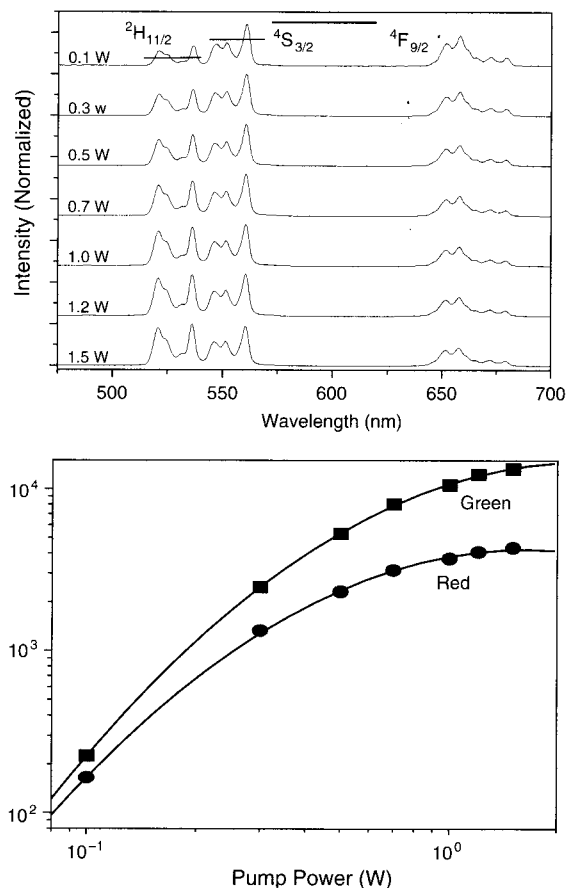


Fig. 19. UCL spectra under various excitation powers in $\text{Gd}_2\text{O}_3\text{:2% Yb}^{3+}$, 1% Er^{3+} NW. Inset: ln-ln plot of emission intensity versus excitation power.

make the nonradiative relaxation processes such as $^4I_{11}-^4I_{13}$ effective, leading to the variation of the intensity of the red to the green emissions. The present intensity ratio variation of the UCL transitions to the IR transitions of $^4I_{13}-^4I_{15}$ should occur for the same reason.

Figure 19a shows the UCL spectra under the excitation with different powers. It can be seen that the intensity ratio of red emissions to green emissions had only a little variation with excitation power. On the other hand, the intensity ratio of $^2H_{11/2}-^4I_{15/2}$ to that of $^4S_{13/2}-^4I_{15/2}$ increased with the increasing excitation power. This was attributed to the thermal effect caused by absorbing the 808-nm light. The energy level of $^2H_{11/2}$ and $^4S_{13/2}$ is quite close ($\sim 340\text{ cm}^{-1}$). The thermal distribution will dominate the population distribution of the two levels, which is much faster than any radiative and nonradiative transitions. Therefore, the intensity ratio of $^2H_{11/2}-^4I_{15/2}$ to $^4S_{13/2}-^4I_{15/2}$ is a critical parameter to the thermal effect. Figure 19b shows the emission intensity for the red and the green emissions as a function of excitation powder. The red and green emissions increased quickly at the original period, then increased slowly, and finally approached a saturation value. This can be mainly attributed to the competition between linear decay and up-conversion processes for the depletion of the intermediate excited states.^{41,42} In nanosized particles, due to the increase of nonradiative relaxation processes, the competition becomes intense. The thermal effect may also contribute to the intensity variation. Generally, the thermal effect leads to an increase of temperature and the quenching of fluorescence.

4. CONCLUSIONS

Different oxide nanowires such as monoclinic LaPO_4 , hexagonal La_2O_3 , and cubic Gd_2O_3 doped with different RE (RE = Eu^{3+} , Tb^{3+} , Ce^{3+} , Yb^{3+} , Er^{3+}) were prepared by the wet-chemical technique. Their luminescent properties such as local environments, electronic transitions, ET, and frequency UCL were systemically studied.

In $\text{LaPO}_4:\text{Eu}^{3+}$ NWs, two groups of emission lines were discerned, corresponding to different symmetry sites. This was attributed to the degenerated crystal field in the fringe edge along the length axis. In NP and MP, only one group of emission lines was observed. In $\text{La}_2\text{O}_3:\text{Eu}^{3+}$ NWs, three sites were discerned, while in MRs two sites/local environments were discerned. The symmetry sites/local environments in $\text{La}_2\text{O}_3:\text{Eu}^{3+}$ NWs differ obviously from that in MRs. In wirelike powders, the local environments of RE ions demonstrate remarkable differences from those in NP and MP, which may be caused by the shape anisotropy.

In $\text{LaPO}_4:\text{Eu}$ NWs, it was observed that the electronic transition rates of the $^5D_1-\Sigma^7F_J$ increased ~ 2 times compared to the corresponding NPs, MPs, and MRs, while that of $^5D_0-\Sigma^7F_J$ increased 1.5 times. This was attributed to the variation of dipole field due to the shape anisotropy.

The nonradiative transition rate of $^5D_1-^5D_0$ in NWs had only a little increase compared to those of MPs and MRs, while that in NPs increased obviously. Therefore, the luminescent QE in NWs was enhanced remarkably compared to that in NPs, MPs, and MRs. This behavior demonstrates that RE doped in 1D NWs is a promising path to improve the luminescent QE of some oxide phosphors. Of course, this does not mean efficient luminescent nanowires can be obtained in any case.

In $\text{LaPO}_4:\text{Ce}^{3+}/\text{Tb}^{3+}$ NWs, the electronic transition rate of $\text{Ce}^{3+}/\text{Tb}^{3+}$ had only a little variation in comparison to the MRs. The ET rate from Ce^{3+} to Tb^{3+} decreased remarkably. Fortunately, in $\text{Ce}^{3+}/\text{Tb}^{3+}$ co-activated LaPO_4 NWs, the brightness for the green emissions of Tb^{3+} increased greatly compared to that in MRs due to decreased energy loss in the excited states higher than 5D_0 of Tb^{3+} .

In $\text{Gd}_2\text{O}_3:\text{Yb}^{3+}/\text{Er}^{3+}$ powders, the UCL increased as the shape of nanomaterials varied from nanopapers to NWs, while the IR luminescence of $^4I_{13}-^4I_{15}$ decreased remarkably. This demonstrates that efficient UCL can be obtained by modifying the shape of nanomaterials.

Acknowledgments: We gratefully thank the financial support of the "One Hundred Talents Project" from Chinese Academy of Sciences and the National Natural Science Foundation of China (Grant No. 10374083).

References and Notes

1. A. Trave, F. Buda, and A. Fasolino, *Phys. Rev. Lett.* 77, 5405 (1996).
2. J. R. Agger, M. W. Anderson, M. E. Pemble, O. Terasaki, and Y. Nozue, *J. Phys. Chem. B* 102, 3345 (1998).
3. R. N. Bhargava, D. Gallagher, and A. N. Hong, *Phys. Rev. Lett.* 72, 416 (1994).
4. J. Yu, H. Liu, Y. Wang, F. E. Fernandez, W. Jia, L. Sun, C. Jin, D. Li, J. Liu, and S. Huang, *Opt. Lett.* 22, 913 (1997).
5. S. B. Qadra, E. F. Skelton, and D. Hsu, *Phys. Rev. B* 60, 9194 (1999).
6. K. Riwotzki and M. Haase, *J. Phys. Chem. B* 102, 916 (1998).
7. B. Bihari, H. Eilers, and B. M. Tissue, *J. Lumin.* 75, 1 (1997).
8. G. A. Conde, R. M. Garcia, and C. I. Hernandez, *Appl. Phys. Lett.* 78, 3436 (2001).
9. K. S. Hong, R. S. Meltzer, and B. Bihari, *J. Phys. Chem. B* 102, 916 (1998).
10. R. S. Meltzer and K. S. Hong, *Phys. Rev. B* 61, 3396 (2000).
11. R. S. Meltzer, S. P. Feofilov, and B. Tissue, *Phys. Rev. B* 60, R14012 (1999).
12. D. K. Williams, H. Yuang, and B. M. Tissue, *J. Lumin.* 83, 297 (1999).
13. H. Peng, H. Song, B. Chen, J. Wang, S. Lu, and J. Zhang, *Chem. Phys. Lett.* 370, 485 (2003).
14. Z. Wei, L. Sun, C. Liao, X. Jiang, and C. Yan, *J. Phys. Chem.* 106, 10 610 (2002).
15. C. Jia, L. Sun, F. Luo, X. Jiang, L. Wei, and C. Yan, *Appl. Phys. Lett.* 84, 5305 (2004).
16. Z. Wei, L. Sun, C. Liao, and C. Yan, *Appl. Phys. Lett.* 80, 1447 (2002).
17. W. P. Zhang, P. B. Xie, C. K. Duan, K. Yan, M. Yin, L. R. Lou, S. D. Xia, and J. C. Krupa, *Chem. Phys. Lett.* 292, 133 (1998).

18. D. Matsuura, *Appl. Phys. Lett.* 81, 4526 (2002).
19. J. A. Capobianco, F. Vetrone, J. C. Boyer, A. Speghini, and M. Bettinelli, *J. Phys. Chem. B* 106, 1181 (2002).
20. F. Vetrone, J. C. Boyer, J. A. Capobianco, A. Speghini, and M. Bettinelli, *J. Phys. Chem. B* 107, 1107 (2003).
21. H. Song, B. Chen, H. Peng, and J. Zhang, *Appl. Phys. Lett.* 81, 1776 (2002).
22. J. Wang, H. Song, B. Sun, X. Ren, B. Chen, and W. Xu, *Chem. Phys. Lett.* 379, 507 (2003).
23. H. Peng, H. Song, B. Chen, J. Wang, S. Lu, and X. Kong, *J. Chem. Phys.* 118, 3277 (2003).
24. H. Song, J. Wang, B. Chen BJ, and S. Lu, *Chem. Phys. Lett.* 376, 1 (2003).
25. H. Song, B. Chen, B. Sun, J. Zhang, and S. Lu, *Chem. Phys. Lett.* 372, 368 (2003).
26. S. Iijima, *Nature (London)* 354, 56 (1991).
27. X. F. Daun, Y. Huang, Y. Cui, J. F. Wang, and C. M. Lieber, *Nature (London)* 409, 66 (2001).
28. E. C. Dickey, C. A. Crimes, M. K. Jain, K. G. Ong, D. Qian, P. D. Kichambare, R. Andrews, and D. Jacques, *Appl. Phys. Lett.* 79, 4022 (2001).
29. H. Kind, H. Yan, M. Law, B. Messer, and P. Yang, *Adv. Mater. (Weinheim, Ger.)* 14, 158 (2002).
30. Y. C. Kong, D. P. Yu, B. Zhang, W. Fang, and S. Q. Feng, *Appl. Phys. Lett.* 78, 4 (2001).
31. Y. Cui, Q. Wei, H. Park, and C. M. Lieber, *Science (Washington, D.C., U.S.)* 299, 1874 (2003).
32. D. D. Ma, C. S. Lee, F. C. K. Au, S. Y. Tong, and S. T. Lee, *Science (Washington, D.C., U.S.)* 293, 1289 (2003).
33. H. Meyssamy, K. Riwotzki, A. Kornowski, S. Naused, and M. Haase, *Adv. Mater.* 11, 840 (1999).
34. M. Yada, M. Mihara, S. Mouri, and T. Kijima, *Adv. Mater.* 14, 309 (2002).
35. C. Wu, W. Qin, G. Qin, D. Zhao, J. Zhang, and S. Huang, *Appl. Phys. Lett.* 82, 520 (2003).
36. H. Song, L. Yu, S. Lu, T. Wang, Z. Liu, and L. Yang, *Appl. Phys. Lett.* 85, 470 (2004).
37. L. Yu, H. Song, and S. Lu et al., *J. Phys. Chem.*, in press.
38. U. Rambabu and S. Buddhudu, *J. Opt. Mat.* 17, 401 (2001).
39. U. R. Munirathmam, T. L. Prakash, and S. Buddhudu, *J. Phys. Chem.* 78, 160 (2003).
40. O. Moune, P. Porcher, and P. Caro, *J. Solid State Chem.* 50, 41 (1983).
41. S. Singh and J. E. Geusic, *Phys. Rev. Lett.* 17, 865 (2004).
42. M. Pollnau, D. R. Gamelin, S. R. Luthi, and H. U. Gudel, *Phys. Rev. B* 61, 3337 (2000).

Received: 13 December 2004. Accepted: 24 January 2005.